ELSEVIER

International Journal of Solids and Structures 41 (2004) 2919–2938

INTERNATIONAL JOURNAL OF SOLIDS and STRUCTURES

www.elsevier.com/locate/ijsolstr

Fracture simulation for anisotropic materials using a virtual internal bond model

Ganesh Thiagarajan *, Anil Misra

Department of Civil Engineering, University of Missouri-Kansas City, 350J Flarsheim, 5100 Rockhill Road, Kansas City, MO 64110, USA

Received 11 November 2003; received in revised form 5 December 2003

Available online 27 February 2004

Abstract

A virtual internal bond (VIB) model for isotropic materials has been recently proposed to describe material deformation and fracture under static and dynamic loading situations. Fracture simulation using an isotropic VIB model, is made possible by incorporating a cohesive type law, inspired by atomistic-level interaction among particles into a hyper-elastic framework at the continuum level. Thus, fracture is built directly into the constitutive formulation. The numerical implementation of the model into a finite element scheme and the determination of model material parameters was described in detail in [Eng. Fract. Mech. 71 (2004) 401].

In this paper, the isotropic model is extended for the fracture simulation of anisotropic materials. This is done by introducing a bond density function at the atomistic level, that can model a variety of anisotropic materials. The bond density function is modeled by spherical harmonics expansions. The derived anisotropic model is implemented as a material model subroutine in ABAQUS and used to perform fracture simulations in anisotropic materials. Simulations and results of comparisons with the isotropic model are presented in this paper.

Keywords: Cohesive model; Anisotropic material fracture; Crack propagation; Finite elements

1. Introduction

The prediction and numerical simulation of fracture in a variety of materials ranging from brittle to ductile materials, composite materials, functionally graded materials, etc. is at the fore front of research in modern times. With the availability of advanced computational technologies the numerical simulation of fracture to predict crack initiation, growth and propagation has made significant advances. There are three primary approaches to the problem of fracture simulation.

The first approach is based on a molecular dynamics (MD) method, where the inter-atomic potentials are used to simulate millions of atoms with appropriate boundary conditions. At times the MD method is

* Corresponding author. Tel.: +1-816-235-1288; fax: +1-816-235-1260.
E-mail addresses: ganesht@umkc.edu (G. Thiagarajan), misraa@umkc.edu (A. Misra).

0020-7683/$ - see front matter © 2004 Elsevier Ltd. All rights reserved.
doi:10.1016/j.ijsolstr.2004.01.013

coupled with the finite element method to make the problem tractable. The MD method depends critically on an appropriate choice of the inter-atomic potential and the availability of supercomputing facilities. For example, Abraham et al. (1994) have used MD method to study the instability dynamics of fracture of brittle materials and Broughton et al. (1998) have investigated the numerical simulation of fracture of silicon using a coupled molecular dynamics and finite element approach.

The second approach is based on using cohesive surfaces in a finite element scheme. Barenblatt (1959), Dugdale (1960), Willis (1967) and others have addressed issues pertaining to this approach. Needleman (1987) provided a framework for the separation process starting from initial debonding in the cohesive zone. Larsson (1995) used this approach to simulate fracture in brittle materials while Xia and Shih (1995) simulated fracture in ductile materials under static loading. Xu and Needleman (1994) introduced special boundary elements, between regular elements, which obey a cohesive stress-separation law. The factors that influence the cohesive law behavior are the cohesive strength and the fracture energy in the separation process. These models obviate the need for a separate fracture criterion, but can allow cracks to form only along the element boundaries. Gullerud and Dodds (1999) and Foulk et al. (2000) have more recently used the 3-D cohesive elements in between regular finite elements in the fracture zone, known a priori, to model crack behavior in ductile materials and composites, respectively.

The third approach, which is also based on a finite element method, has two important features that differentiate it from the other two approaches. Firstly, it is a multi-scale approach that bridges the atomistic and continuum scales and secondly it incorporates fracture criterion directly into the constitutive formulation of the material. The first feature allows it to incorporate features of the atomistic level interactions, such as inter-particle potentials, while the second feature implies that no crack zones and paths need to be specified a priori, consequently no boundary elements are needed. This approach was first proposed by Gao (1996, 1997) for materials undergoing brittle fracture, based on his theory that a hyper-elastic description, in the Lagrangian framework, of the crack tip behavior provides a better explanation of crack tip instabilities. Gao and Klein (1998) later developed a method called the virtual internal bond (VIB) model, in which a cohesive type law is directly incorporated into the constitutive model by treating the body as a collection of randomly oriented material points interconnected by a network of cohesive bonds. The Cauchy–Born rule of crystal elasticity is used to derive the overall constitutive relations by equating the strain energy of the bonds to the potential energy stored in the continuum due to applied loads and deformations. The bridging of scales between the continuum and atomistic levels is done by relating the bond length between the atoms to the continuum based Green–Lagrange strain tensor. The 2nd Piola-Kirchoff stress tensor can then be computed from the potential energy expression.

The VIB model may be implemented into the finite element methods based on two integration schemes, namely the implicit and the explicit schemes. Klein and Gao (1998) used an implicit second-order time stepping algorithm to successfully simulate quasi-static and dynamic loading problems. Zhang et al. (2002) used the implicit integration scheme and implemented the VIB model in ABAQUS (ABAQUS, 2000) using the UMAT subroutine.

The softening region of the constitutive model presents certain problems when using the implicit integration schemes with elliptic equations, which arise as the formulation correlates the onset of fracture to the presence of strain localization caused by the loss of ellipticity of the governing equations. The loss of ellipticity could result in singular tangent matrices and the associated presence of negative eigen-values. Thus, a successful implementation of the implicit integration scheme could require preconditions, such as the incorporation of stiff elements adjoining the VIB layer elements or specification of a narrow band of VIB layer, which is akin to prespecifying the crack path.

To avoid the numerical issues posed by the implicit integration scheme, the VIB model was implemented for dynamic problems in an explicit integration scheme by Thiagarajan et al. (2004). The model was successfully implemented in ABAQUS using the VUMAT subroutine to study the effect of mesh size and loading rates on crack initiation, propagation and branching. The experimental verification and validation

of the VIB model has been studied for the dynamic fracture and fragmentation of brittle materials under impact loading in Thiagarajan et al. (2002, 2004). Good agreement was shown between the predicted and experimentally determined values.

The motivation for the current study stems from the necessity to propose a similar methodology for predicting the crack initiation, propagation and branching for anisotropic materials. Anisotropy is introduced as a directional distribution of the bond density function, recognizing that the bond densities are different in different directions. In this paper, the bond density function is modeled by using spherical harmonic expansions. In the subsequent discussions we present the theoretical details of the anisotropic VIB model to simulate fracture in anisotropic materials. The numerical implementation and results for an anisotropic plate with a hole problem are then presented. These results are compared with those for isotropic materials to highlight the effect of anisotropy on fracture propagation.

2. Anisotropic VIB model: theoretical formulation

The basic premise of the VIB model as proposed by Gao (1996, 1997) and Gao and Klein (1998), is that the elastic behavior of a spatial distribution of material points at the continuum level is related to the underlying atomistic-level cohesive bonds through the Cauchy–Born rule of crystal elasticity. The interaction at the atomistic level may be described through interaction potentials.

2.1. VIB model framework

The VIB model is described within the framework of hyper-elastic continuum mechanics. The initial and the deformed configurations are defined using the Lagrangian coordinates $\mathbf{X} = X_I$ and the Eulerian coordinates $\mathbf{x} = \mathbf{x}(\mathbf{X}, t) = x_i(X_I, t)$, respectively. In this paper, capital letter subscripts are used for the initial configuration while lower case subscripts are used for the deformed configuration. The deformation gradient can be expressed as follows

$$\mathbf{F} = \frac{\partial \mathbf{x}}{\partial \mathbf{X}} \quad \text{or } F_{iI} = \frac{\partial x_i}{\partial X_I} \tag{1}$$

The Green–Lagrange strain tensor may then be defined as

$$\mathbf{E} = \frac{1}{2}(\mathbf{F}^{\mathrm{T}} \cdot \mathbf{F} - \mathbf{I}) \tag{2}$$

where $\mathbf{I}$ is the second-order identity tensor.

Consider an arbitrary micro-structural bond at an angle θ and ϕ, where θ is the angle of the bond orientation with respect to the vertical positive 2-axis, and ϕ is the angle in the horizontal plane with respect to the positive 1-axis, respectively. The unit vector along this direction is given as $\xi = (\sin\theta\cos\phi, \sin\theta\sin\phi, \cos\theta)$ with respect to the undeformed configuration. The stretch of this bond can be given as

$$l = l_0\sqrt{1 + 2\xi_I E_{IJ}\xi_J} \tag{3}$$

The macroscopic strain energy density function is derived using the Cauchy–Born rule (Milstein, 1980; Tadmor et al., 1996) as

$$\psi(E_{IJ}) = \langle U(l) \rangle \tag{4}$$

where $\langle \cdots \rangle$ represents the weighted average with respect to the bond density function D_{d} and $U(l)$ is the bond potential energy function. Assuming that all bonds have the same initial length l_0, for the general case the weighted average is given as,

$$\langle \cdots \rangle = \int_0^{2\pi} \int_0^{\pi} \ldots D_{\mathrm{d}}(\theta, \phi) \sin\theta \mathrm{d}\theta \mathrm{d}\phi \tag{5}$$

The term $D_{\mathrm{d}}(\theta, \phi) \sin(\theta)\, \mathrm{d}\theta\, \mathrm{d}\phi$ represents the number of bonds per unit volume between the bond angles (θ, $\theta + \mathrm{d}\theta$) and ($\phi$,$\phi + \mathrm{d}\phi$).

2.2. Bond density functions

The anisotropy in the VIB fracture model is introduced in Eq. (5) through the inclusion of density functions that characterizes the directional dependence of the bond density. The bond density requires a density function in spherical polar coordinates that can describe the concentrations of bond orientation. Spherical harmonics expansions may be used to represent such bond orientation densities (Chang and Misra, 1990; Misra, 1999).

The bond density function, $D_{\mathrm{d}}(\theta, \phi)$, may be expressed as a spherical harmonics expansion as follows

$$D_{\mathrm{d}}(\theta, \phi) = \frac{1}{4\pi} \left(1 + \sum_{k=2}^{\infty'} \left[a_{k0} P_k(\cos\theta) + \sum_{m=1}^{k} P_k^m(\cos\theta)(a_{km} \cos(m\phi) + b_{km} \sin(m\phi)) \right] \right) \tag{6}$$

where θ and ϕ are as defined earlier. Furthermore, $\sum'$ represents the summation with respect to even indices only; $P_k(\cos\theta)$ is the kth Legendre polynomial; $P_k^m(\cos\theta)$ is the associated Legendre function; and a_{k0}, a_{km}, and b_{km} are coefficients of spherical harmonics expansions. In order to ensure that the density function is centrosymmetric, and symmetric about the $z = 0$ plane (i.e. $D_{\mathrm{d}}(\theta, \phi) = D_{\mathrm{d}}(\pi - \theta, \phi + \pi)$ and $D_{\mathrm{d}}(\theta, \phi) = D_{\mathrm{d}}(\pi - \theta, \phi)$), only the even harmonics are admissible. The first term in Eq. (6) represents a sphere and the subsequent terms can be regarded as a function defined on the surface of the sphere. Since the Legendre polynomials and the associated Legendre functions are orthogonal to 1, it follows that Eq. (6) is a density function such that

$$\int_{\Omega} D_{\mathrm{d}}(\theta, \phi) \mathrm{d}\Omega = 1 \tag{7}$$

For simplicity of the subsequent formulation, a truncated form of the expansion of Eq. (6), consisting of second-order terms, is used. The Legendre polynomial of degree two, i.e. $P_2(\cos\theta)$ is given by Abramowitz and Stegun (1965)

$$P_2(\cos\theta) = \frac{1}{2}(3\cos^2\theta - 1) \tag{8}$$

The associated Legendre function $P_2^2(\cos\theta)$ can be obtained from the Rodrigues formula (Abramowitz and Stegun, 1965) as follows

$$P_k^m(x) = \frac{(1 - x^2)^{\frac{m}{2}}}{2^k k} \frac{\mathrm{d}^{k+m}}{\mathrm{d}x^{k+m}} (x^2 - 1)^k \tag{9}$$

For $k = 2$ and $M = 2$ Eq. (9) yields

$$P_2^2(\cos\theta) = 3\sin^2\theta \tag{10}$$

Thus, the truncated spherical harmonics expansion consisting of second-order terms is finally given as

$$D_{\mathrm{d}}(\theta, \phi) = \frac{1}{4\pi} \left[1 + \frac{1}{4} a_{20}(3\cos 2\theta + 1) + 3\sin^2\theta (a_{22} \cos 2\phi + b_{22} \sin 2\phi) \right] \tag{11}$$

2.3. Material symmetries

By choosing appropriate values of coefficients a_{20}, a_{22} and b_{22} different types of material symmetries can be simulated. The case for isotropic and transversely isotropic materials is described here.

Isotropic material: For example, $a_{20} = a_{22} = b_{22} = 0$ represents an isotropic material, as the bond density function becomes a constant. In this case the macroscopic strain energy function is given as

$$\psi(E_{IJ}) = D_{\mathrm{d}} \int_0^{2\pi} \int_0^{\pi} U(l) \sin\theta \, \mathrm{d}\theta \, \mathrm{d}\phi \tag{12}$$

where $D_{\mathrm{d}} = \frac{1}{4\pi}$ from Eq. (11), which is identical to the isotropic VIB model as proposed by Gao (1996, 1997) and Gao and Klein (1998).

Transversely isotropic material: For transversely isotropic materials, the coefficients $a_{22} = b_{22} = 0$ and a_{20} is the only non-zero coefficient. Furthermore, for transversely isotropic materials, the density function must be positive semi definite, that is $D_{\mathrm{d}} \geqslant 0$, for all values of θ and ϕ. Therefore

$$1 + \frac{a_{20}}{4}(3\cos 2\theta + 1) \geqslant 0 \tag{13}$$

which results in the coefficient a_{20} being bounded as follows

$$-1 \leqslant a_{20} \leqslant 2 \tag{14}$$

The coefficient a_{20} represents the shape of the density distributions; $a_{20} = -1$ represents the case where the bonds are concentrated in the 1- and 3-directions and gradually decrease to none in the 2-direction. On the other extreme, $a_{20} = 2$ represents the case where the bonds concentrate along the 2-direction. Fig. 1 gives a pictorial representation of the bond density functions for four different values of a_{20}.

2.4. Constitutive equations and cohesive force law

From the strain energy density function ψ given in Eq. (4), the symmetric 2nd Piola-Kirchoff stress S_{IJ} and the elastic modulus C_{IJKL} can be derived as follows

$$\mathbf{S} = \frac{\partial \psi}{\partial \mathbf{E}} \quad \text{or } S_{IJ} = \frac{\partial \psi}{\partial E_{IJ}} \tag{15}$$

$$C_{IJKL} = \frac{\partial^2 \psi}{\partial E_{IJ} \partial E_{KL}} \tag{16}$$

The modulus derived from this potential satisfies the major and minor symmetries, $C_{IJKL} = C_{JIKL} = C_{IJLK} = C_{KLIJ}$, as well as the Cauchy symmetry, $C_{IJKL} = C_{IKJL}$. For isotropic material this results in only one elastic constant being needed. This is due to the fact that the Cauchy symmetry is satisfied by the fourth-order isotropic elasticity tensor only for the case of $\lambda = \mu$, where λ and μ are the two Lame's constants.

While it is very difficult to derive a closed form solution for the elastic stiffness tensor for a general case, Gao and Klein (1998) have derived analytical forms of the elastic stiffness tensor for a few simple cases. These cases serve as a guideline to correlate isotropic material properties to the model parameters. For the plane stress isotropic solid it was shown by Gao and Klein (1998) that the shear modulus is given by

$$\mu = \frac{\pi D_0 l_0^2 U''(l_0)}{4} \tag{17}$$

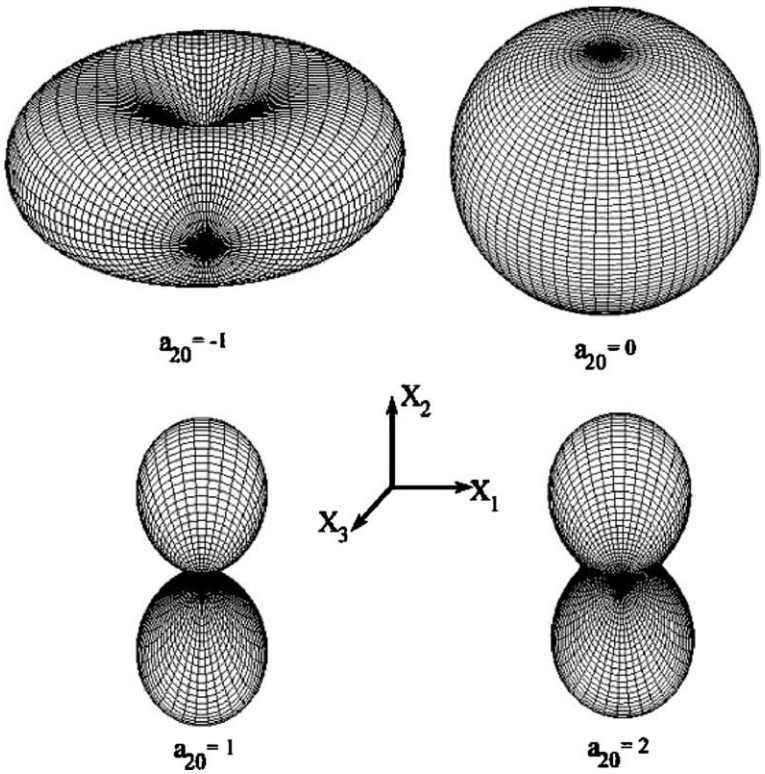

Fig. 1. Bond density function representations for $a_{20} = 2.0$, 1.0, 0.0 and −1.0.

In this paper we utilize the classical two parameter cohesive force law expressed as

$$U'(l) = A_a(l - l_0)\mathrm{e}^{-\frac{l-l_0}{B_b}} \tag{18}$$

and is represented in Fig. 2. $U'(l)$ is the cohesive force and is the derivative of the bond potential energy with respect to the bond length 'l'. Under the case of equibiaxial stretching, the constant A_a can be related to the initial shear modulus by Eq. (17) and represents the initial slope of the curve in Fig. 2. The parameter $\frac{l-l_0}{B_b}$ is related to the strain at which the cohesive stress is reached and is determined by matching the experimental results with numerical simulations and is described in detail in Thiagarajan et al. (2004). A brief description is given in this paper in the section on the determination of parameters.

2.5. Elastic properties for tranversely isotropic material

The analytical expressions for the elastic properties using the anisotropic VIB model can be derived for a few simple cases as shown below. For transversely isotropic materials the coefficients reduce to $a_{22} = b_{22} = 0, a_{20} \neq 0$.

Infinitesimal strain case: For the infinitesimal strain case the Green–Lagrange strain and the 2nd P.K. Stress tensor reduce to the stress and strain tensors of linear elasticity. For this case the potential function can be expanded up to the second term as shown below

$$\psi = \left\langle U(l_0) + \frac{l_0^2}{2}U''(l_0)(\xi_i\epsilon_{ij}\xi_j)(\xi_k\epsilon_{kl}\xi_l) \right\rangle \tag{19}$$

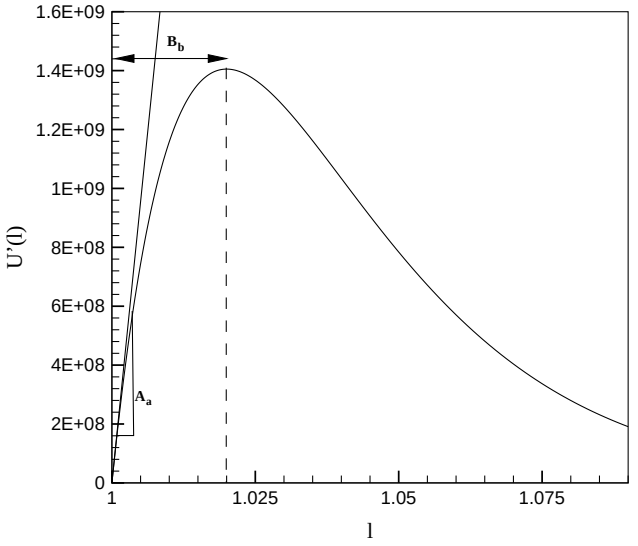

Fig. 2. Representation of 2-parameter cohesive law.

From Eq. (19) the fourth-order elasticity tensor can be derived using Eq. (16) and expressed as follows

$$C_{ijkl} = \langle U''(l_0)(\xi_i \epsilon_{ij} \xi_j)(\xi_k \epsilon_{kl} \xi_l) \rangle \tag{20}$$

$$= \int_0^{2\pi} \int_0^{\pi} l_0^2 U''(l_0) D_{\mathrm{d}}(\theta, \phi)(\xi_i \xi_j \xi_k \xi_l) \sin\theta \, \mathrm{d}\theta \, \mathrm{d}\phi \tag{21}$$

where $D_{\mathrm{d}}(\theta, \phi)$ is given by Eq. (11). Using the expression for the cohesive force, as shown in Eq. (18), the non-zero components of the initial material tangent moduli can be expressed as shown here. Defining K_n as

$$K_n = -\frac{A\mathrm{e}^{\left(-\frac{l-l_0}{B}\right)}(-B + l - l_0)}{B} \tag{22}$$

the moduli can be expressed as follows

$$\begin{aligned}
C_{2222} &= \frac{K_n l_0^2 D}{5}\left(1 + \frac{4a_{20}}{7}\right) \\
C_{2211} &= \frac{K_n l_0^2 D}{5}\left(\frac{1}{3} + \frac{a_{20}}{35}\right) \\
C_{1111} &= -\frac{K_n l_0^2 D}{5}\left(1 + \frac{2a_{20}}{7}\right) \\
C_{1133} &= -\frac{K_n l_0^2 D}{5}\left(\frac{1}{3} + \frac{2a_{20}}{3}\right) \\
C_{3333} &= -\frac{K_n l_0^2 D}{5}\left(1 + \frac{2a_{20}}{7}\right) \\
C_{2121} &= \frac{K_n l_0^2 D}{5}\left(\frac{1}{3} + \frac{a_{20}}{35}\right) \\
C_{2323} &= \frac{K_n l_0^2 D}{5}\left(\frac{1}{3} + \frac{a_{20}}{35}\right) \\
C_{1313} &= \frac{K_n l_0^2 D}{5}\left(\frac{1}{3} + \frac{2a_{20}}{35}\right)
\end{aligned} \tag{23}$$

It can be shown that $C_{2233} = C_{1122} = C_{3322} = C_{2211}$ and $C_{3311} = C_{1133}$. In addition, the symmetries due to the transversely isotropic material $C_{2323} = C_{2233}$ and $C_{1133} = C_{1313}$ may be observed in the above equations. The five elastic constants for a transversely isotropic material are of the form shown below.

$$\begin{aligned} E_{\mathrm{L}} &= \frac{(880a_{20}^3 + 273a_{20}^2 - 6468a_{20} - 6860)}{105(73a_{20}^2 - 392 - 112a_{20})}K_n \\ E_{\mathrm{T}} &= \frac{(80a_{20}^2 - 77a_{20} - 490)}{105(13a_{20} + 28)}K_n \\ \nu_{\mathrm{LT}} &= \frac{7(5a_{20} + a_{20}^2 - 14)}{(73a_{20}^2 - 112a_{20} - 392)} \\ \nu_{\mathrm{TT}} &= \frac{(a_{20} + 7)}{(13a_{20} + 28)} \\ G_{\mathrm{T}} &= \left(\frac{a_{20}}{105} + \frac{1}{15}\right)K_n \\ G_{\mathrm{LT}} &= \left(\frac{a_{20}}{105} + \frac{1}{15}\right)K_n \end{aligned} \tag{24}$$

Figs. 3 and 4 show the variation of the longitudinal E_{L} and the transverse E_{T} elastic moduli, for a transversely isotropic material with the strain $\frac{l-l_0}{B}$ for different a_{20} values. Two observations can be made from these figures. Firstly, the modulus E_{L} decreases and E_{T} increases as a_{20} decreases. Secondly, the moduli in both cases decreases to zero with increasing strain of $\frac{l-l_0}{B}$ up to 1.0 and then become negative which represents the softening phase.

Fig. 5 shows the variation of two Poisson's ratios ν_{LT} and ν_{TT}, in the longitudinal–transverse and transverse–transverse directions with the parameter a_{20}. It can be observed that for the isotropic case $a_{20} = 0$ the ratios are 0.25 which corresponds to the isotropic VIB case.

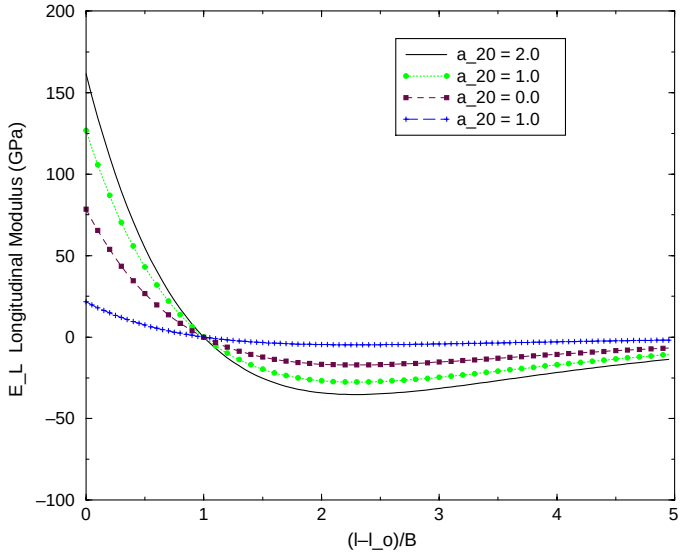

Fig. 3. Variation of E_{L} with $\frac{l-l_0}{B}$ for different a_{20}.

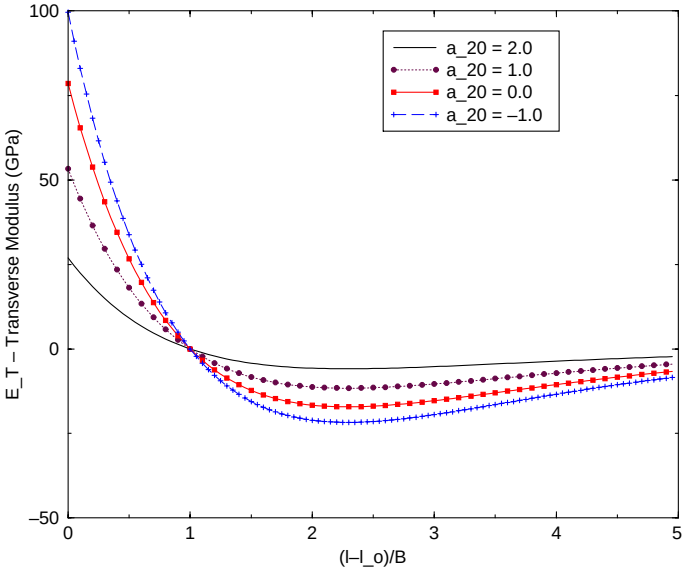

Fig. 4. Variation of E_{T} with $\frac{l-l_0}{B}$ for different a_{20}.

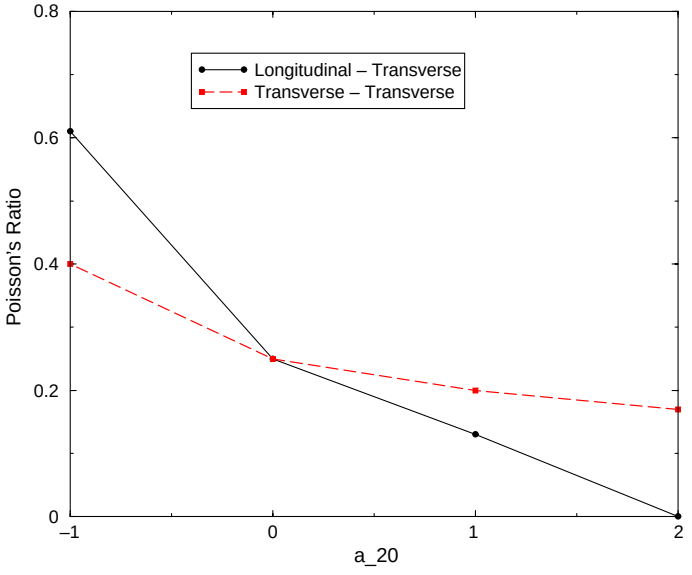

Fig. 5. Variation ν_{LT} and ν_{TT} for different a_{20}.

Equitriaxial stretching case: The Green–Lagrange strain tensor components for the case of equitriaxial stretching case can be expressed as $E_{IJ} = \epsilon\delta_{IJ}$. The deformation gradient reduces to a diagonal form as follows

$$F_{11} = F_{22} = F_{33} = \sqrt{1+2\epsilon} \tag{25}$$

Using the deformation gradient shown in Eq. (25) the bond length is given as

$$l = l_0\sqrt{1+2\epsilon} \tag{26}$$

Substituting the bond length in the cohesive force equation gives,

$$U'(l_0\sqrt{1+2\epsilon}) = -\frac{A(l_0\sqrt{1+2\epsilon}-l_0)\mathrm{e}^{\left(-\frac{l_0\sqrt{1+2\epsilon}-l_0}{B}\right)}}{l_0\sqrt{1+2\epsilon}} \tag{27}$$

The expressions for the non-zero 2nd Piola-Kirchoff stresses can now be expressed using Eq. (15) as follows:

$$S_{22} = \frac{1}{15}\frac{A\mathrm{e}^{\left(\frac{l_0}{B}\right)}(-5+2\sqrt{1+2\epsilon}a_{20}-2a_{20}+5\sqrt{1+2\epsilon})}{\mathrm{e}^{\left(\frac{l_0\sqrt{1+2\epsilon}}{B}\right)}\sqrt{1+2\epsilon}} \tag{28}$$

$$S_{11} = \frac{1}{15}\frac{A\mathrm{e}^{\left(\frac{l_0}{B}\right)}(5\sqrt{1+2\epsilon}-\sqrt{1+2\epsilon}a_{20}-5+a_{20})}{\mathrm{e}^{\left(\frac{l_0\sqrt{1+2\epsilon}}{B}\right)}\sqrt{1+2\epsilon}} \tag{29}$$

$$S_{33} = S_{11} \tag{30}$$

It has seen that the stresses in the two transverse directions are equal. It can be shown from a graphical representation that the cohesive S_{22} stress decreases and the cohesive S_{11} stress increases, as the parameter a_{20} is decreased from 2 to -1.

3. Results and discussions

For general loading conditions the anisotropic VIB model, given by Eqs. (15) and (16), is numerically evaluated to study the dependency of the stress–strain behavior on the anisotropy coefficient a_{20}. The model is also implemented into the finite element program ABAQUS, as a material VUMAT subroutine to investigate crack initiation and propagation. In the subsequent discussions, the cohesive force law parameters are first determined, the effect of anisotropy on the stress strain curve then presented and finally the finite element results of the plate with a hole problem is described.

3.1. Determination of cohesive force law parameters

The material used for realistic simulations in this study, is chosen as one with an elastic modulus in the principal axis of anisotropy (2-direction), $E_{22} = 370$ GPa and a mass density of $\rho = 3960$ kg/m^3. This choice is made to allow for comparisons of crack patterns with the isotropic VIB simulations given in Thiagarajan et al. (2004). The parameter A_a in Eq. (18) which represents the initial slope of the cohesive stress separation curve, can be computed using the following equation

$$A_a = \frac{4}{\pi}\frac{1}{D_0 l_0^2}\mu \tag{31}$$

where μ is the shear modulus of an isotropic material. The parameter $\frac{l-l_0}{B_b}$ in Eq. (18) represents the strain at which the cohesive stress is reached. It has been found in Thiagarajan et al. (2004), using experimental verifications and validation, that the parameter $\frac{l-l_0}{B_b}$ is representative of the strain at which brittle materials fracture. For the material chosen in the simulations presented in this paper a value of 0.0025 is chosen for the parameter B_b, which is similar to that used by Thiagarajan et al. for the case of isotropic alumina (Thiagarajan et al., 2004). Furthermore, D_0 and l_0 is taken as unity.

3.2. Validation of model parameters

Andrews and Kim (1988) have studied some of the issues relating to dynamic fracture and fragmentation in brittle materials under impact loading. They conducted tests on small spherical balls made of alumina impacting a rigid anvil. Four different particle diameters (0.795, 1.59, 3.18 and 6.35 mm) were tested to investigate the effect of particle size on the fragmentation process.

One set of data (0.795 mm ball diameter) was used to calibrate the VIB model parameters (A_a and B_b). The value of A_a is computed as outlined in Eq. (31). For the impact simulations the parameter B_b (which represents the strain at which the cohesive stress is reached) was determined by matching the threshold velocity of 50 m/s reported (Andrews and Kim, 1988, Fig. 4a). A finite element mesh with three noded plane stress triangular elements was used for the alumina disk. The anvil was modeled using rigid link elements. The disk had 276 nodes and 500 elements. A velocity initial condition was specified for the disk and simulations were run with different values of the parameter B_b.

It was found from the simulations (Thiagarajan et al., 2004) that a value of B_b in the range of 0.0015–0.0025 resulted in the threshold velocity of 50 m/s. Values of B_b greater than 0.0025 did not result in fracture at 50 m/s. As B_b was lowered the first value that predicted the fracture was chosen. A value of $B_b = 0.0015$ shows multiple cracks immediately after the bounce while the simulation with a $B_b = 0.0025$, showed one central crack just appearing. Hence a value of $B_b = 0.0025$ was chosen for subsequent validations of the model. It is interesting to note that this range of B_b represents the range of strains at which brittle materials such as alumina fracture (as the VIB model originally assumed).

Numerical verification: To verify the validity of the VIB model the simulations were run for the other two diameters (1.59 and 6.35 mm). Numerical simulations were also done for a 4mm diameter disk. The values of A_a and B_b determined for the 0.795 mm diameter ball were used in these simulations. The disks were impacted at different velocities. The primary purpose was to determine the threshold velocity for each disk, called the critical impact velocity. It was shown in Thiagarajan et al. (2004) that the model predictions agree well with the experimental results (Andrews and Kim, 1988).

3.3. Effect of anisotropy on the stress–strain curves

A displacement controlled single element uniaxial strain simulation, along the major axis (y-axis), was performed using the proposed anisotropic VIB model to study the stress–strain curves predicted for transversely isotropic materials using four different values of the coefficient a_{20}. These four different values of the coefficient $a_{20} = -1$, 0, 1, and 2 represent different bond density functions as shown in Fig. 1. The corresponding stress–strain responses for the four cases are shown in Fig. 6. It is observed that as a_{20} increases, the cohesive stress increases significantly which is the result of an increase in the bond density in the y-direction. In all these simulations the strain at which the cohesive stress is reached is kept the same, by retaining the same value of B_b.

The nature of stresses in the transverse (x- and z)-directions were also studied for the case of a uniaxial strain in the longitudinal (y)-direction. The evolution of the transverse stress due to the loading in the longitudinal direction is shown in Fig. 7 from which the following important observations may be made.

1. Firstly, it can be seen that the stress in the longitudinal direction reaches its cohesive limit earlier than the transverse direction stresses. From Fig. 7 it is also observed that the transverse stress continues to increase even when the longitudinal stress is in the softening region. Thus the transverse stress reaches the maximum (or "cohesive limit") at a higher strain, which depends upon the anisotropy parameter a_{20}.
2. Secondly, as the coefficient a_{20} decreases, the transverse direction softens at a faster rate. Thus the faster softening rate is observed, as seen in Fig. 7, by the rate at which the stress ratio curve goes back to zero once the stresses in both the directions have reached their respective cohesive limits.

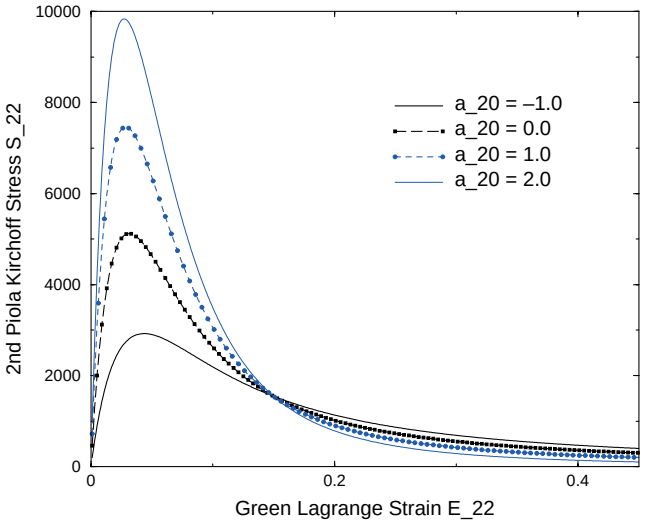

Fig. 6. Comparison of stress–strain for single element simulation.

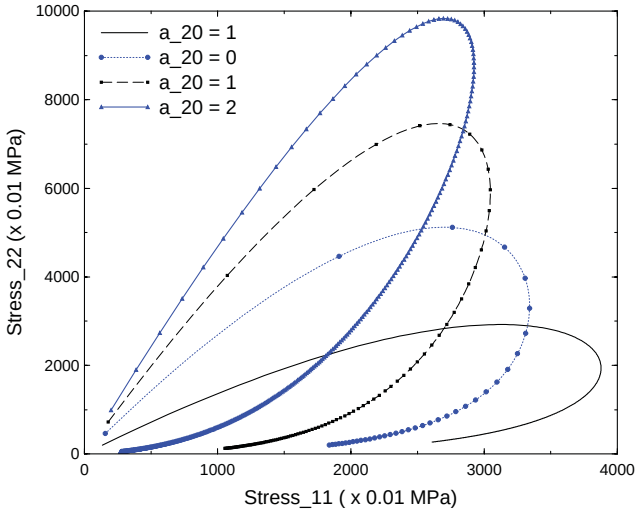

Fig. 7. Stress ratios in 2-directions for single element simulation.

Therefore, the effect of anisotropy parameter a_{20} on the strain at the cohesive stress limit is studied using Figs. 8 and 9, which show the variation of the average and the deviatoric stress with the longitudinal Green–Lagrange strain, respectively. As seen in Fig. 8, the maximum average stress, defined as $(\frac{\sigma_1+\sigma_2}{2})$, occurs at different strains depending upon the initial anisotropy. In addition, the post peak softening response in terms of the average stress also depends upon the initial anisotropy. The material with higher stiffness in the longitudinal direction has a steeper softening regime as opposed to the material with a higher stiffness in the transverse direction. Fig. 9, which is a plot of the deviatoric stress, defined as $(\frac{\sigma_1-\sigma_2}{2})$, versus the longitudinal strain shows that the post peak deviatoric stresses diminish to zero at smaller strains for material with higher stiffness in the longitudinal direction. Clearly the indication is that the material does

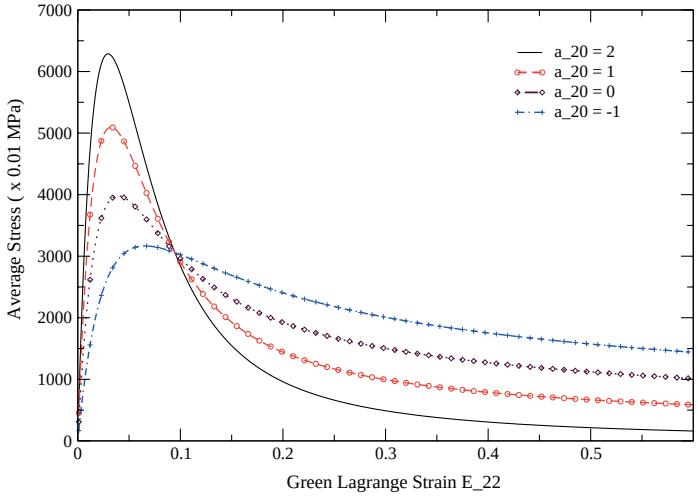

Fig. 8. Average stress–longitudinal strain for single element simulation.

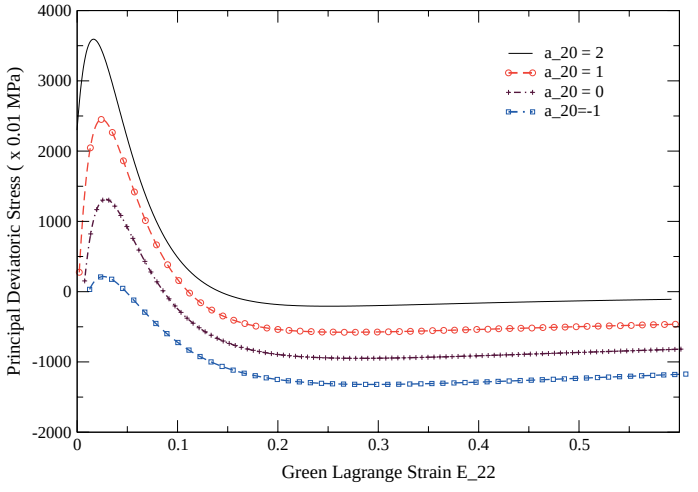

Fig. 9. Deviatoric stress–longitudinal strain for single element simulation.

not fail in the transverse direction (direction perpendicular to the loading). To obtain the orientation of failure plane a bifurcation analysis would be needed which would be pursued in a separate publication.

Fracture energy due to change in a_{20}: The fracture energy for different values of the parameter a_{20}, has been computed here as the energy based on stress–strain curves in Fig. 6. Fig. 10 shows the variation of the fracture energy for different a_{20} values. It is observed that the fracture energy increases linearly with an increase in a_{20} from -1 to 2.

3.4. Plate with a hole simulation results

The anisotropic VIB model described in the previous section, has been incorporated into a user material model subroutine in ABAQUS. The implementation is done using the VUMAT subroutine of ABAQUS,

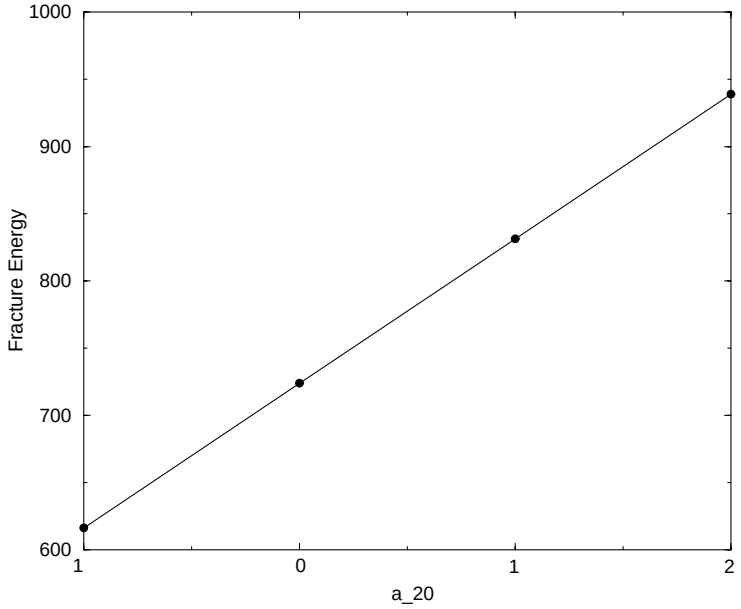

Fig. 10. Variation of fracture energy with a_{20}.

the explicit integration scheme and the Cauchy stress components. As the stresses and strains are defined in the corotational system, the stress and other state variables can be computed directly and updated in the subroutine. ABAQUS provides, among other quantities, the strain increments and the deformation gradient at the current time increment.

The resulting model has been used to study a plate with a hole subjected to displacement loading in the vertical direction, as shown in Fig. 11. The mesh contains 4712 nodes and 2250 eight noded brick elements with a reduced integration scheme. There are two layers of elements in the thickness direction. Plane stress elements were not used in order to utilize the three dimensional feature of the anisotropic VIB model. Only an eighth of the plate is simulated due to symmetry conditions. The displacement is gradually increased from 0% to 20% of the vertical dimension in 1 s.

The fracture initiation and patterns are generated by the finite element simulations for four different cases of the coefficient a_{20}. The stress–strain results from the first element on the lowest row and located adjacent to the hole (bottom corner) are compared with those of the uniaxial strain simulation results, in Fig. 12, for the case of the coefficient $a_{20} = 0$ and 2 . The stress–strain behaviors are obtained from the uniaxial strain and finite element simulations compare very well. The difference in the peak cohesive stress values indicate that the loading condition in the finite element simulation is not purely uniaxial strain.

Normalization factor for time: The normalization factor for time to be used in anisotropic problems, such as the one described in this paper, may be defined as the time required for the stress wave to travel the length of the plate, and is given as

$$\delta t = \frac{L}{c_{\mathrm{d}}} \tag{32}$$

where c_{d} is the wave speed and L is the length of the plate. The wave speed c_{d} may be expressed as

$$c_{\mathrm{d}} = \sqrt{\frac{E_{\mathrm{L}}}{\rho}} \tag{33}$$

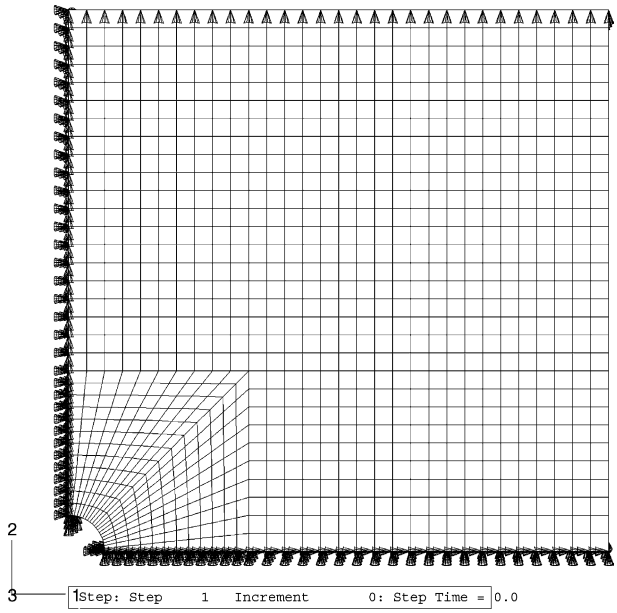

Fig. 11. Mesh used in plate with hole simulations.

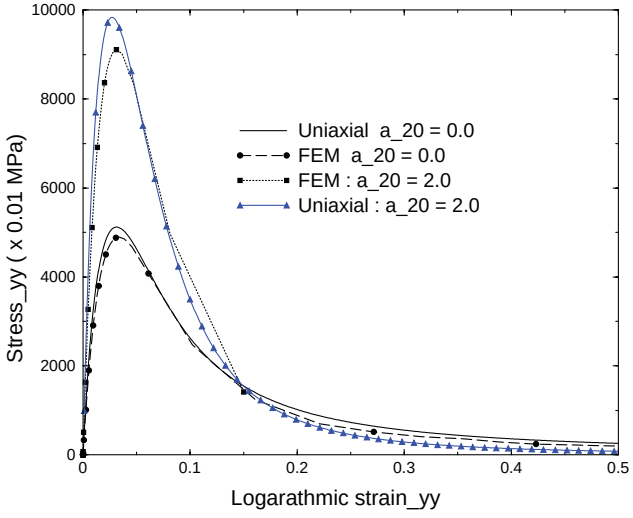

Fig. 12. Comparison of stress–strain for corner element (FEM/single element simulation).

where E_L is the longitudinal modulus given by Eq. (24). Since E_L is dependent on the anisotropy parameter a_{20} the wave speeds vary with a_{20}. Hence, it is not possible to have the same normalization number for all the simulations. The normalization factor used for results shown in Fig. 13 is the δt value that corresponds to the parameter $a_{20} = 0$—the isotropic case. However, in Fig. 15 where the onset of crack appearance for different values of a_{20} is compared, two different factors are used. One of them is the constant scaling factor with $a_{20} = 0$ and the other represents the variable scaling factor wherein δt is computed directly from Eq. (32) which varies for different values of a_{20}.

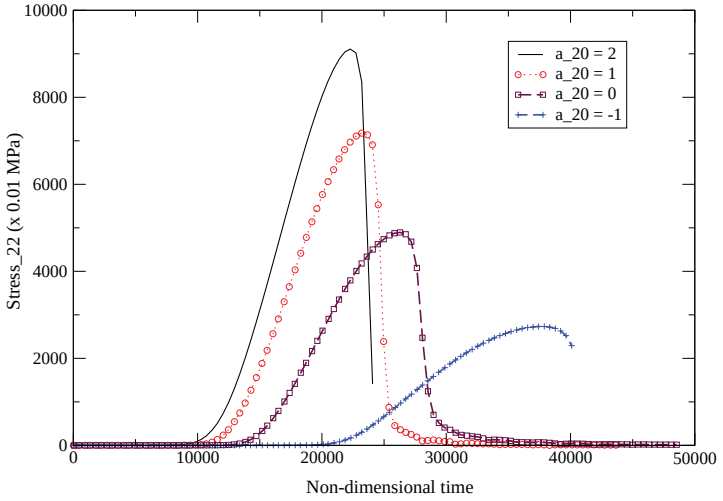

Fig. 13. Stress (2-2) variation with time (at the corner element).

The results from the left bottom corner element, adjacent to the hole, has been studied for the variation of stresses with time. Fig. 13 shows the variation of the longitudinal stress with time for the four different values of the coefficient a_{20}. The vertical axis in Fig. 13 represents the stress value while the horizontal axis represents the normalized time value. As explained earlier in this section, the normalization time factor used here corresponds to the wave speed of the isotropic material $a_{20} = 0$. Fig. 14 shows the variation of the longitudinal stress along the path defined by the bottom edge of the plate. In Fig. 15, which shows the normalized time value at which the stress in this element reaches its cohesive limit, two different normalization factors are used. The constant scaling factor corresponds to the isotropic material whereas the variable scaling factor, which is truly representative of the actual time required for the wave to travel one length of the plate, depends on the value a_{20}. The following observations can be made from Figs. 13–15.

1. The time for the element to be stressed increases as a_{20} decreases as seen in Fig. 13. The increase is due to the fact that the time required for the stress wave to propagate is related to the elastic modulus of the material in the longitudinal direction. As the elastic modulus decreases with a_{20}, the time required for the element to be stressed increases.
2. From Fig. 13 it is noted that the peak or cohesive stress limit drops as the coefficient a_{20} decreases.
3. From Fig. 14 it is observed that the stress concentration depends on the coefficient a_{20}. The concentration decreases with the coefficient a_{20}. These stresses are plotted at their respective crack initiation times. As expected the stress in the vertical direction also decreases with a_{20}.
4. The time—using the constant scaling factor curve as shown in Fig. 15—at which the cohesive stress limit is reached increases as the coefficient a_{20} decreases. This point is further illustrated using the deformed mesh for the different cases, which are shown in Figs. 16 ($a_{20} = 2.0$), 17 ($a_{20} = 0.0$) and 18 ($a_{20} = -1.0$). All the deformations shown are at identical times. The material with $a_{20} = 2$ is most heavily cracked while that with $a_{20} = -1$ has not yet cracked at this time.
5. The difficulties associated with an appropriate choice of the time scaling parameter is clearly illustrated in Fig. 15, which shows the crack initiation times using constant and variable scaling factors. The constant scaling curve gives an intuitively correct representation, that the time for crack initiation should increase with a decrease in the longitudinal modulus. However, the variable scaling curve appears to give the opposite result. For the variable scaling case, although the scaled value decreases, the scaling factor

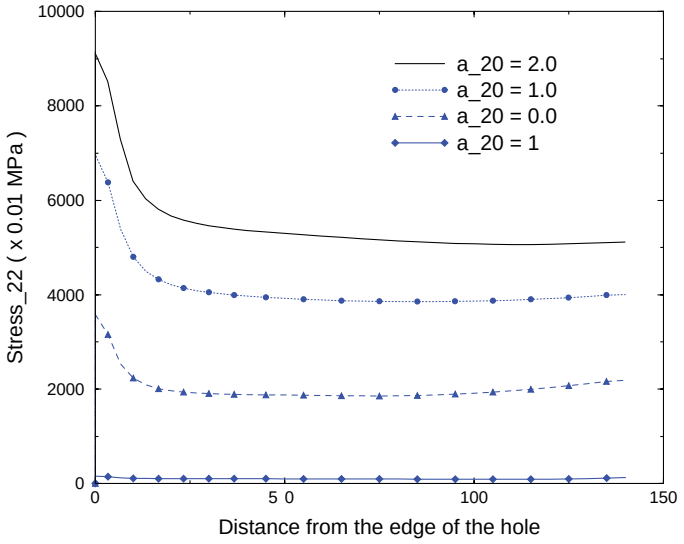

Fig. 14. Stress (2-2) variation with distance from the corner element.

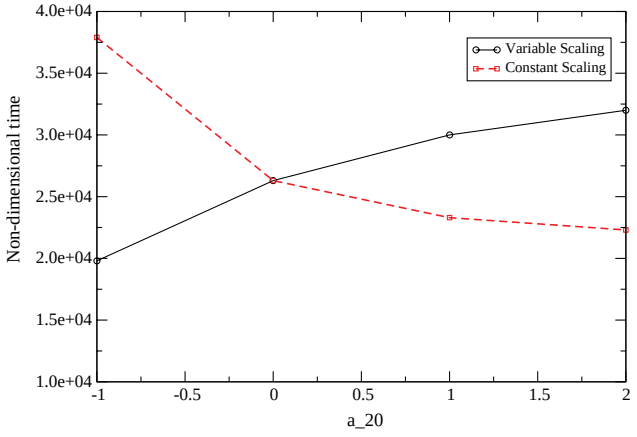

Fig. 15. Crack initiation times for the four a_{20} cases.

increases with a decrease in a_{20}, and the product of the two quantities, which gives the actual time for the crack, shows an increase.

Another important issue in dynamic fracture mechanics is the prediction of the crack tip velocity. For quasi brittle materials the theory predicts that the limiting fracture speed is the Rayleigh wave speed. However, the experimentally determined values are much lower (of the order or 0.3–0.33 of the Rayleigh wave speed). The VIB model, in principle, has been shown to provide an explanation to this phenomenon by Gao (1996) by developing a concept of local limiting speed for dynamic crack propagation. The numerical implementation of the VIB model could be potentially used to numerically determine the crack tip speeds in order to explain this principle.

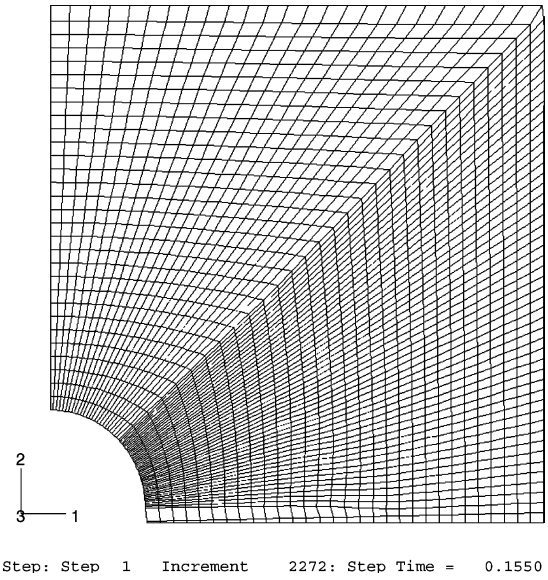

Fig. 16. Fracture pattern of anisotropic plate with $a_{20} = 2.0$.

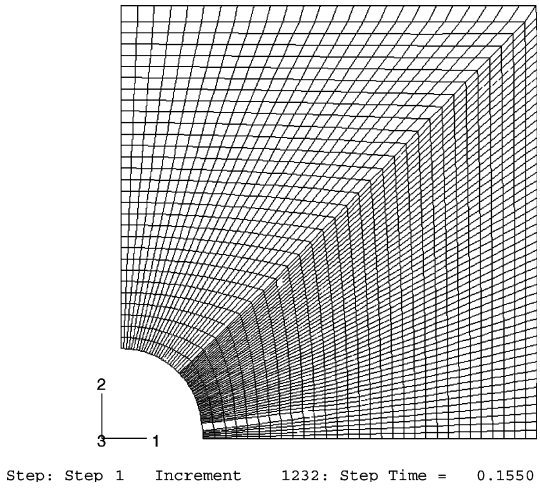

Fig. 17. Fracture pattern of isotropic plate $a_{20} = 0.0$.

4. Conclusions

In this paper, an extension of the VIB model is presented for the finite element simulation of crack initiation and propagation for anisotropic materials. The anisotropy of the material is modeled using bond density functions, represented by spherical harmonics and is built in a multi-scale framework wherein the energy due to atomistic bonds are related to the continuum energy. The extended model is used to derive closed form expressions for (1) the anisotropic material moduli under small strain condition and (2) stress–

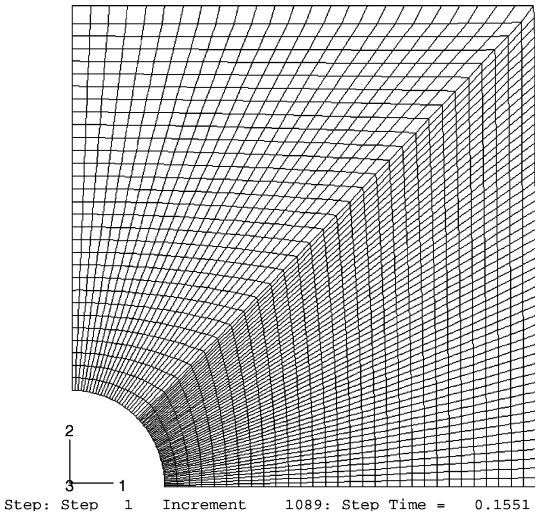

Fig. 18. Fracture pattern of anisotropic plate with $a_{20} = -1.0$.

strain behavior under equitriaxial stretching. From the results presented in this paper the following conclusions are drawn.

1. The cohesive stress limit depends on the nature of anisotropy. As the number of bonds increase in a particular direction, the cohesive stress limit also increases. This has been shown here both from single element and finite element simulations.
2. As the bond density increases in a particular direction the elastic modulus also increases, resulting in an increase in the wave speed. Consequently, the time for crack initiation depends upon the nature of initial anisotropy. Under longitudinal loading, the crack initiates earlier for material with higher stiffness in the longitudinal direction.
3. The postpeak response is also a function of the initial anisotropy. Fracture simulation results show that under longitudinal loading a material with higher stiffness in the longitudinal direction has a steeper softening regime.
4. Based upon single element calculations of transverse stress behavior under uniaxial longitudinal strain we note that the failure orientation is likely to depend on the initial anisotropy.
5. The finite element implementation in an explicit integration scheme with ABAQUS/Explicit is very robust, in that the softening region in modeled numerically to its completion without instabilities. Consequently very large deformations may occur facilitating the modeling of crack initiation and propagation.
6. The model builds in the fracture criterion into the constitutive model, thereby eliminating the necessity of any external fracture criterion or any cohesive spring elements in between element boundaries.

Acknowledgements

Ganesh Thiagarajan would like to acknowledge the National Center for Supercomputing Applications (NCSA) at the University of Illinois at Urbana Champaign for the computational resources used under the project award OND and the University of Missouri Research Board (UMRB) for supporting this project.

References

Abraham, F.F., Brodbeck, D., Rafey, R.A., Rudge, W.E., 1994. Instability dynamics of fracture: a computer simulation investigation. Physical Review Letters 272.

Abramowitz, M., Stegun, I.A., 1965. Handbook of Mathematical Functions. Dover, New York, NY.

Andrews, E.W., Kim, K.S., 1988. Threshold conditions for dynamic fragmentation of ceramic particles. Mechanics of Materials 29, 161–180.

Barenblatt, G.I., 1959. The formation of equilibrium cracks during brittle fracture: general ideas and hypotheses, axially symmetric cracks. Applied Mathematics and Mechanics (PMM) 23, 622–636.

Broughton, J.Q., Bernstein, N., Kaxiras, E., Abraham, F.F., 1998. Concurrent coupling of length scales: methodology and applications. Physical Review B 60, 2391.

Chang, C.S., Misra, A., 1990. Packing structure and mechanical properties of granulates. Journal of Engineering Mechanics, ASCE 116 (5), 1077–1093.

Dugdale, D.S., 1960. Yielding of steel sheets containing silts. Journal of Mechanics and Physics of Solids 8, 100–104.

Foulk, J.W., Allen, D.H., Helms, K.L.E., 2000. Formulation of a three dimensional cohesive zone model for application to a finite element algorithm. Computer Methods in Applied Mechanics in Engineering 183, 51–66.

Gao, H., 1996. A theory of local limiting speed in dynamic fracture. Journal of Mechanics and Physics of Solids 44, 1453–1474.

Gao, H., 1997. Elastic waves in a hyperelastic solid near its plane strain equibiaxial cohesive limit. Philosophical Magazine Letters 76, 307–314.

Gao, H., Klein, P., 1998. Numerical simulation of crack growth in an isotropic solid with randomized internal cohesive bonds. Journal of Mechanics and Physics of Solids 46 (2), 187–218.

Gullerud, A., Dodds, R., 1999. 3-D modelling of ductile crack growth in thin sheet metals. Engineering Fracture Mechanics 63, 347–374.

H.K.S. Inc. 2000. ABAQUS/Standard and ABAQUS/Explicit Users Manual.

Klein, P., Gao, H., 1998. Crack nucleation and growth as strain localization in a virtual internal bond continuum. Engineering Fracture Mechanics 61, 21–48.

Larsson, R., 1995. A generalized fictitious crack model based on plastic localization and discontinuous approximation. International Journal for Numerical Methods in Engineering 38, 3167–3188.

Milstein, F., 1980. Review: theoretical elastic behavior at large strains. Journal of Material Science 15, 1071–1084.

Misra, A., 1999. Micromechanical model for anisotropic joints. Journal of Geophysical Research 104 (810), 175–187.

Needleman, A., 1987. A continuum model for void nucleation by inclusion debonding. Journal of Applied Mechancis 54, 525–531.

Tadmor, E.B., Ortiz, M., Phillips, R., 1996. Quasicontinuum analysis of defects in solids. Philosophical Magazine A 73, 1529–1563.

Thiagarajan, G., Hsia, J.K., Huang, Y.Y., 2002. Experimental verification and validation of the virtual internal bond model for dynamic fracture. Annual Meeting, Society of Engineering Sciences, State College, PA.

Thiagarajan, G., Hsia, J.K., Huang, Y.Y., 2004. Finite element implementation of virtual internal bond model for simulating crack behavior. Engineering Fracture Mechanics 71, 401–423.

Willis, J.R., 1967. A comparison of the fracture criteria of Griffith and Barenblatt. Journal of Mechanics and Physics of Solids 15, 151–162.

Xia, L., Shih, F.C., 1995. Ductile crack growth. I. A numerical study using computational cells with microstructurally based length scales. Journal of Mechanics and Physics of Solids 43 (2), 233–259.

Xu, X.P., Needleman, A., 1994. Numerical simulation of fast crack growth in brittle solids. Journal of Mechanics and Physics of Solids 42 (9), 1397–1434.

Zhang, P., Klein, P., Huang, Y., Gao, H., Wu, P.D., 2002. Numerical simulation of cohesive fracture by the virtual internal bond method. Computer Modeling in Engineering and Sciences 3, 263–278.